J. Fluid Mech. (2022), *vol*. 944, A19, doi:10.1017/jfm.2022.470

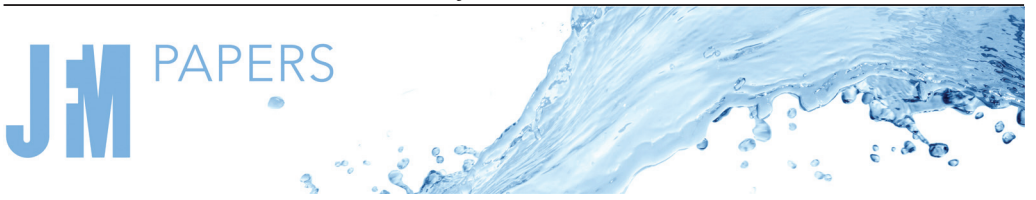

Hydrodynamic performance of oscillating elastic propulsors with tapered thickness

Ersan Demirer[1], **Oluwafikayo A. Oshinowo**[2], **Alper Erturk**[1] and **Alexander Alexeev**[1],†

[1]George W. Woodruff School of Mechanical Engineering, Georgia Institute of Technology, Atlanta, GA 30332, USA

[2]Daniel Guggenheim School of Aerospace Engineering, Georgia Institute of Technology, Atlanta, GA 30332, USA

(Received 9 August 2021; revised 1 March 2022; accepted 17 May 2022)

Using fluid–structure interaction computational modelling, the hydrodynamic performance of bio-inspired elastic propulsors with tapered thickness that oscillate in an incompressible Newtonian fluid at Reynolds number $Re = 2000$ is investigated. The thickness tapering leads to an acoustic black hole effect at the trailing edge of the propulsor that slows down and attenuates flexural waves, thereby minimizing the flexural wave reflection and enhancing travelling wave propulsion. The simulations reveal that, by tuning the propulsor thickness profile modulating the acoustic black hole effect, the tapered propulsors can be designed to vastly outperform the uniformly thick propulsors in terms of the hydrodynamic efficiency and thrust, especially for the post-resonance frequencies. The enhanced hydrodynamic performance is directly linked to the ability of the tapered propulsors to generate travelling waves with a large amplitude displacement at the trailing edge. The results have implications for the development of highly efficient bio-mimetic robotic swimmers and, more generally, the better understanding of the undulatory aquatic locomotion.

Key words: swimming/flying, propulsion, flow-structure interactions

1. Introduction

From anguilliform with the undulatory locomotion based on travelling waves to ostraciiform mainly using standing waves, fish swimming can be categorized by the type of wave propagation (Gray 1933). By analysing films of fish locomotion, Gray (1933) identified and described wave mechanisms creating forward thrust. Following this fish swimming categorization, Lighthill (1960) showed that the nature of the propagating wave

† Email address for correspondence: alexander.alexeev@me.gatech.edu

directly affects the swimming efficiency. Standing wave-based propulsion can generate substantial thrust, whereas travelling wave propulsion is generally more efficient at intermediate Reynolds numbers (Cui *et al.* 2018).

Fish demonstrate a wide variety of beating patterns by leveraging their muscles and body elasticity. Furthermore, fish can dynamically vary the beating parameters including the wavenumber, amplitude, velocity and the ratio of travelling and standing waves (Bowtell & Williams 1991). When it comes to man-made swimming devices, the generation and control of complex beating patterns are challenging tasks. Although travelling waves improve the efficiency of hydrodynamic propulsion, it is not trivial to generate travelling waves in a passive finite-size propulsor. When a wave propagates from one end of a plate, its reflection at the other end creates a backward wave. When the incident and reflected waves superpose, a standing wave emerges.

Several approaches were suggested to yield travelling waves in finite-size structures, including active and passive solutions (Roh, Lee & Han 2001; Kósa, Shoham & Zaaroor 2005; Kim, Park & Jeong 2009). Hariri, Bernard & Razek (2013) used pairs of piezoelectric patches along a beam to actively maintain a travelling wave in the finite-size beam. While one piezoelectric patch generates the wave, the paired patch dissipates the propagating wave by converting the mechanical energy into electrical energy. By impeding the reflection of incident waves at the tip of the beam, the system actively suppresses the generation of standing waves. In an alternative passive approach, dissipation can be used to damp the propagation of the incident wave which suppresses the wave reflection and facilitates the formation of travelling waves. Ramananarivo, Godoy-Diana & Thiria (2013) demonstrated that fluid dissipation allows an artificial swimmer to generate travelling waves. In this case, the surrounding viscous fluid suppresses the incident wave as it propagates along the swimmer and thus mitigates the reflection at the free end. However, while the dissipation prevents standing wave formation, it also leads to a low beating amplitude, which in turn results in limited efficiency and propulsion.

Another passive approach to create travelling flexural waves in finite-size elastic structures is based on the use of structures with gradually decreasing thickness, such as tapered beams (Mironov 1988). When beam thickness decreases, wave speed reduces and goes to zero in the limit of the zero-thickness beam tip, leading to a region where waves are trapped. This phenomenon is referred to as an acoustic black hole (ABH) due to the analogy with celestial black holes. ABH prevents the wave reflection resulting in the formation of travelling waves and the suppression of standing waves. ABH devices have been studied for applications in vibration absorption (Feurtado, Conlon & Semperlotti 2014; Conlon, Fahnline & Semperlotti 2015), sound attenuation (Bowyer & Krylov 2015) and energy harvesting (Zhao, Conlon & Semperlotti 2015). Note that the ABH effect can be enhanced by applying a thin absorbing layer onto the plate surface for dissipation (Krylov & Tilman 2004).

Fins and rays typically feature a tapered geometry with the thickness and stiffness gradually decreasing from the fin base to the trailing edge (Alben, Madden & Lauder 2007; Lauder *et al.* 2007; Aiello, Westneat & Hale 2017; Aiello *et al.* 2018). One can speculate that this geometry can be potentially beneficial to enhancing the fin hydrodynamic performance. Experiments show that different stiffness distributions yield diverging swimming behaviours (Aiello *et al.* 2018). Even slight changes in mechanical properties of tapered fins can significantly impact the thrust and lift forces (Tangorra *et al.* 2010). Compared with fins with constant stiffness, the fins with the non-uniform stiffness show clear advantage for undulatory swimming (Kancharala & Philen 2016). Still, no optimal stiffness distribution was identified for maximizing the swimming performance,

highlighting the complex relationship between kinematics, mechanical properties and swimming performance (Feilich & Lauder 2015).

Recent numerical studies confirm the strong effect of the stiffness distribution on the swimming performance (Yeh, Li & Alexeev 2017; Floryan & Rowley 2020; Luo *et al.* 2020). Simulations show that propulsors with tapered thickness widen the range of actuation frequencies yielding high efficiency swimming compared with propulsors with uniform thickness (Yeh *et al.* 2017). The superior performance of tapered propulsors, especially off resonance, is related to their ability to maintain a high tip displacement for a vast range of actuation frequencies. Using a linear inviscid model of an elastic swimmer, it was found that the thrust and power can be respectively maximized and minimized by tuning the stiffness distribution (Floryan & Rowley 2020). Yet, the stiffness distributions optimizing thrust and power are distinctly different. It was suggested that at a finite Reynolds number flow the stiffness distribution leading to the minimum power may converge to that of the maximum thrust, thus yielding an optimal stiffness distribution for the undulatory swimming. Three-dimensional simulations of fins with a cupping stiffness profile show that such fins generate significant thrust while fins with a heterocercal distribution yield higher manoeuvrability (Luo *et al.* 2020). However, the hydrodynamic mechanisms leading to high propulsion or high efficiency remain unclear.

In this work, we use three-dimensional fully coupled numerical simulations to probe the hydrodynamic performance of elastic propulsors with different tapered profiles oscillating in a viscous fluid. We consider propulsor geometries that amplify the ABH effect facilitating the formation of travelling waves propagating along the propulsor. We examine to what extent this effect can be harnessed to enhance the hydrodynamic performance of biomimetic elastic propulsors for undulatory underwater swimming.

The paper is organized as follows. Section 2 describes the definition of the problem, while our computational model and its validation are reported in § 3. Section 4 presents the results of our study and their discussion. We fist examine the ABH effect in finite-size propulsors in § 4.1. The frequency response of propulsors with different tapering geometries is reported in § 4.2. The propulsor bending patterns are examined in § 4.3. In § 4.4, we quantify the effect of ABH on the travelling waves in terms of the travelling-to-standing wave ratio. We then describe propulsor hydrodynamic performance in § 4.5. In § 4.6, we present scaling metrics connecting the propulsor bending pattern with its hydrodynamic performance and show, in particular, that propulsors with ABH exhibit the highest thrust and efficiency. In § 4.7, we present flow patterns typical of tapered propulsors and discuss the hydrodynamic mechanisms enhancing travelling wave locomotion. Our conclusions are summarized in § 5.

2. Problem set-up

We consider a plate propulsor with width W and length L that is composed of two sections: an active section of length L_a with constant thickness h_a and constant stiffness D_a, and a passive attachment of length L_p with variable thickness $h_p(x)$ and variable stiffness $D_p(x)$, as illustrated in figure 1(*a*). The propulsor is clamped at the root and constrained from moving forward. Following Yeh & Alexeev (2016*a*), who showed that internally actuated propulsors with similar configuration are more efficient with passive and active sections of equal length, we set $L_a = 0.5L$. The active section of the plate is internally actuated by a time-varying bending moment $M(t) = M_0 D_a (L_a/W) \sin \omega t$ distributed along the length of the active section that mimics piezoelectric actuation (Yeh & Alexeev 2016*a*; Demirer *et al.* 2021*b*). Here, M_0 is the dimensionless bending moment amplitude and $\omega = 2\pi/\tau$ is

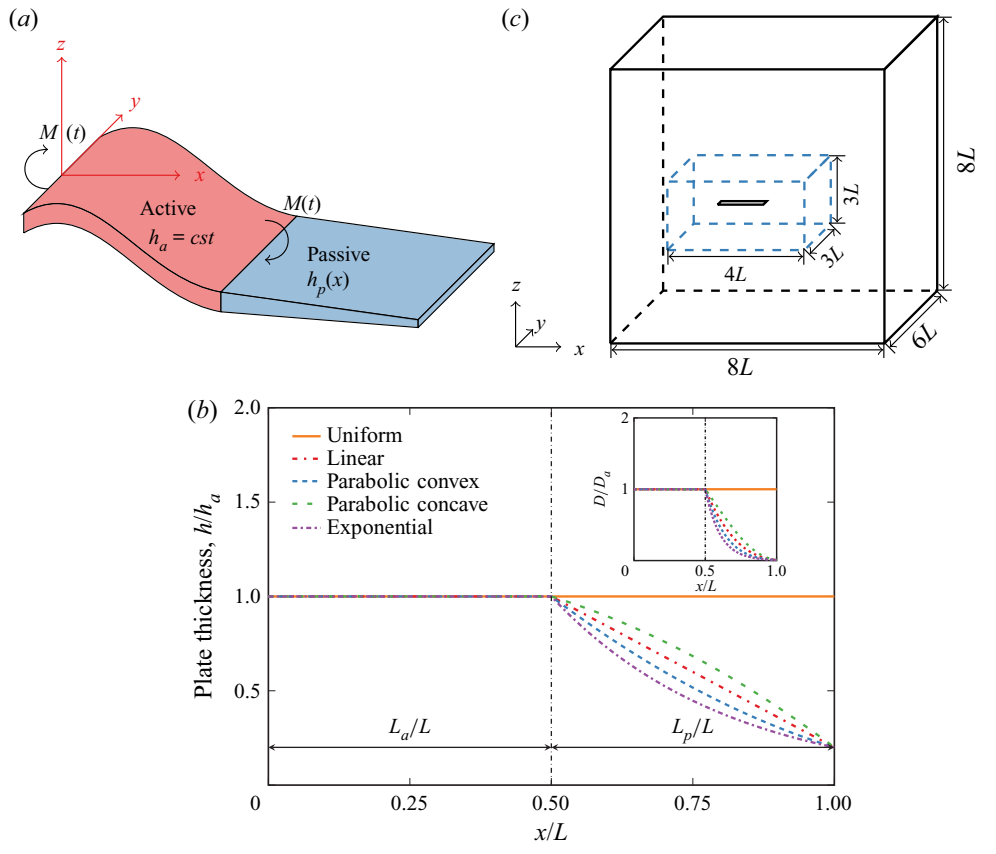

Figure 1. (*a*) Schematics of the internally actuated plate with a tapered attachment. (*b*) Plate thickness distribution along the length for $b = 5$, $L_a/L = 0.5$ and several shapes normalized by the uniform section's properties. The inset shows the resulting stiffness distribution. (*c*) Computational domain consists of a coarse outer mesh and a refined inner mesh around the plate at the centre.

the angular actuation frequency, with τ being the actuation period. To impose a uniform bending moment along the active section, we apply a couple of opposing forces of an equal magnitude distributed along the two edges of the active section (figure 1*a*).

The propulsor thickness is a continuous piecewise-differentiable function ($h \in C^{\infty}_{pw}$)

$$h(x) = \begin{cases} h_a, & \text{for } x \in [0; L_a] \\ h_p(x), & \text{for } x \in]L_a; L] \end{cases}, \tag{2.1}$$

where $h_p(x)$ is a general C^{∞} function defining the 'shape' of the passive attachment tapering. We consider five distinct types of the attachment tapering shapes illustrated in figure 1(*b*) that are referred to as uniform, linear, parabolic convex, parabolic concave and exponential. The corresponding functions are given by

$$h_p(\xi) = \begin{cases} h_a, & \text{uniform}, \\ \dfrac{h_a}{b}[b + (1-b)\xi], & \text{linear}, \\ \alpha\xi^2 + \beta\xi + \gamma, & \text{parabolic}, \\ h_a b^{-\xi}, & \text{exponential}. \end{cases} \tag{2.2}$$

Here, $b = h(L_a)/h(L)$ is the tapering ratio and $\xi = (x - L_a)/L_p$. In the case of the parabolic tapering, additional parameters are

$$\alpha = h_a\left(1 - \frac{1}{b}\right) + \theta, \quad \beta = 2h_a\left(\frac{1}{b} - 1\right) - \theta, \quad \gamma = h_a, \tag{2.3a–c}$$

where θ is the attachment tip slope. We define the convex and concave parabolic shapes by changing the tip slope. We arrange the attachments from the less steep to more steep in the following order: uniform, parabolic concave, linear, parabolic convex and exponential. The stiffness distribution in the propulsors is given by $D(x) = Eh(x)^3/12(1 - \nu^2)$, where E is the Young's modulus and ν is the Poisson ratio (inset in figure 1*b*).

The dynamic response of an oscillating plate is a direct function of the proximity of the actuation frequency to the fundamental resonance. The resonance is defined by the input and response signals being in phase quadrature. The resonance frequency depends on the plate mechanics as well as on the boundary conditions and fluid loading. To characterize the actuation frequency, we define a dimensionless frequency ratio $r = \omega/\omega_r$, where ω_r is the fundamental resonance frequency. When oscillating in a fluid, the volume of the displaced fluid acts as an additional mass which shifts the resonance frequency. The resonance frequency can be estimated as $\omega_r = (\lambda_1^2/L^2)\sqrt{D/(\sigma_s + \sigma_f)}$ (Van Eysden & Sader 2006), where the eigenvalue λ_1 is a function of the aspect ratio, and σ_s and σ_f are the plate mass and added mass per unit area, respectively. In our simulations, we determine ω_r by examining the frequency response function of the plate in fluid. The first peak in tip displacement corresponds to the fundamental resonance. In this work, we explore the propulsor performance for a wide range of frequency ratios $0.7 < r < 3$. To vary r, we keep ω constant and change D through the plate modulus E, thereby altering the resonance frequency ω_r. Indeed, the frequency ratio can be approximated to the first order as $r \simeq \sqrt{D_r/D}$, where D_r is the bending stiffness that yields the resonance (Weaver, Timoshenko & Young 1990). Since D_r is a function of the thickness profile, we recompute D_r for each propulsor geometry. This approach allows us to keep the Reynolds number constant throughout the simulations.

3. Computational model

Our computational model is based on a three-dimensional two-way coupled fluid–structure interaction solver that integrates a lattice Boltzmann model (LBM) for a viscous Newtonian fluid and a finite differences (FD) solver for an elastic solid material. The LBM solves a discrete Boltzmann equation using a computational domain fitted with a cubic lattice of equally spaced nodes. We use a mesh with higher node density near the oscillating plate propulsor to fully resolve the flow, as shown in figure 1(*c*). The flow is characterized by a velocity distribution function $f_i(\boldsymbol{r}, t)$ that represents the density of fluid at position $\boldsymbol{r}$ propagating at velocity $\boldsymbol{c}_i$ in the direction i at time t. We use a D3Q19 lattice that maintains 19 velocity directions of the distribution function in the three spatial dimensions. The time evolution is obtained by integrating the discrete Boltzmann equation (Ladd & Verberg 2001). Macroscopic quantities, such as the density ρ, momentum $\rho\boldsymbol{u}$ and stress $\boldsymbol{\Pi}$ are retrieved by taking moments of the distribution function

$$\rho = \sum_i f_i, \quad \rho\boldsymbol{u} = \sum_i f_i\boldsymbol{c}_i, \quad \boldsymbol{\Pi} = \sum_k f_k\boldsymbol{c}_k\boldsymbol{c}_k. \tag{3.1a–c}$$

The propulsor is modelled as a thin elastic plate that obeys the Kirchhoff–Love theory (Timoshenko & Woinowsky-Krieger 1959). For a plate with inhomogeneous mechanical

properties, the density, thickness and bending stiffness are functions of the position. The differential equation modelling the behaviour of the inhomogeneous elastic plate is given by (Timoshenko & Woinowsky-Krieger 1959)

$$\rho_s h \frac{\partial^2 w}{\partial t^2} = q(x, y, t) + \left(N_x \frac{\partial^2 w}{\partial x^2} + N_y \frac{\partial^2 w}{\partial y^2} + N_{xy} \frac{\partial^2 w}{\partial x \partial y} \right) + \mathcal{L}\,(w, D)\,(x, y, t) - \mathcal{L}\left(\frac{\partial w}{\partial t}, \gamma \right)(x, y, t), \tag{3.2}$$

where w is the transverse displacement, ρ_s is the plate density, h is the thickness, D is the bending stiffness, ν is the Poisson ratio, q is a transverse load, N_x, N_y, N_{xy} are in-plane loads, γ is a Kelvin–Voigt damping and $\mathcal{L}$ is the elastic operator applied to the displacement and bending stiffness (or damping). It is defined as

$$\begin{aligned} \mathcal{L} : (u_1, u_2) \longmapsto & - u_2 \nabla^4 u_1 - \left(\frac{\partial^2 u_2}{\partial x^2} + \nu \frac{\partial^2 u_2}{\partial y^2} \right) \frac{\partial^2 u_1}{\partial x^2} - \left(\frac{\partial^2 u_2}{\partial y^2} + \nu \frac{\partial^2 u_2}{\partial x^2} \right) \frac{\partial^2 u_1}{\partial y^2} \\ & - 2 \frac{\partial^3 u_1}{\partial x^3} \frac{\partial u_2}{\partial x} - 2 \frac{\partial^3 u_1}{\partial y^3} \frac{\partial u_2}{\partial y} - 2 \frac{\partial^3 u_1}{\partial x \partial y^2} \frac{\partial u_2}{\partial x} - 2 \frac{\partial^3 u_1}{\partial x^2 \partial y} \frac{\partial u_2}{\partial y} \\ & - 2(1 - \nu) \frac{\partial^2 u_2}{\partial x \partial y} \frac{\partial^2 u_1}{\partial x \partial y}. \end{aligned} \tag{3.3}$$

Note that, for a plate with homogeneous properties, only the first term of the operator remains, reducing the expression to the classic biharmonic operator.

The fluid and solid models are coupled at the fluid–solid boundaries using a two-way coupling method (Alexeev, Verberg & Balazs 2005; Alexeev & Balazs 2007; Branscomb & Alexeev 2010). A no-slip and no-penetration condition is applied on the moving solid surface by using a linearly interpolated bounce-back rule (Bouzidi, Firdaouss & Lallemand 2001; Chun & Ladd 2007). The momentum exchange approach accounting for the momentum transferred to the plate from the fluid is used to evaluate the hydrodynamic forces on the plate. The resultant hydrodynamic force is distributed to the neighbouring FD nodes using a procedure conserving the force and momentum (Alexeev *et al.* 2005; Demirer *et al.* 2021*b*). Further detail and validation of our computational framework can be found elsewhere (Masoud & Alexeev 2010, 2012; Masoud, Bingham & Alexeev 2012; Mao & Alexeev 2014; Yeh & Alexeev 2014; Yeh *et al.* 2017; Yeh, Demirer & Alexeev 2019; Demirer *et al.* 2021*b*).

To validate our FD solver for modelling the tapered plate mechanics, we evaluate the static deformation of a tapered cantilevered beam with an aspect ratio $\mathcal{A}_R = L/W = 2.5$ due to an external force $q_0 L^2/D_0 = 0.1$ applied at the free end. The beam thickness decreases linearly from the clamped root to the tip with the tapering ratio $b = 5$. In figure 2(*a*), we show the solution for the Poisson ratio $\nu = 0$ using our FD solver that is compared with the Runge–Kutta solution of the governing equation. In the Runge–Kutta solver we use 2000 nodes, whereas the FD solver is tested for two meshes with, respectively, 80×10 and 21×11 nodes. We find that the FD solutions show good agreement with the Runge–Kutta solution, even for relatively large tip deflection of approximately $0.1L$.

In figure 2(*b*), we validate the FD solver using a three-dimensional solution obtained with the finite elements (FE) method using COMSOL Multiphysics. We consider a cantilever beam with $\nu = 0.31$ that has two sections of equal length. The clamped half

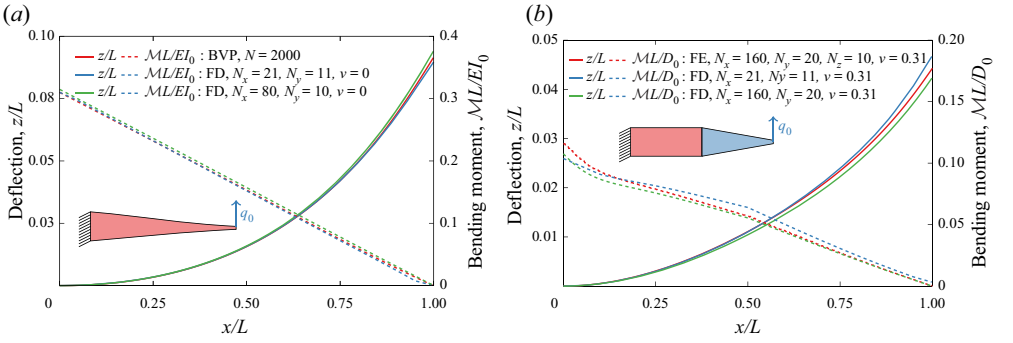

Figure 2. Static deflection under a non-dimensional load $q_0L^2/D_0 = 0.1$ of (*a*) a linearly tapered end-loaded cantilevered beam with $b = 5$ and $\nu = 0$, and (*b*) a beam composed of uniform and linearly tapered sections with $b = 5$ and $\nu = 0.31$.

of the plate has a uniform thickness, while the other half is linearly tapered with a tapering ratio $b = 5$. For the FE solver we use a mesh with 160×20 nodes, while for the FD solver we use meshes with 160×20 and 21×11 nodes. The FD and FE solutions show close agreement. Note that, for a non-zero Poisson ratio, the bending moment shows nonlinear behaviour near the root due to non-negligible two-dimensional effects at the clamped boundary.

The plate oscillations in a viscous fluid are governed by the Reynolds number $Re = \rho U_c L/\mu$, and the mass ratio $\chi = \rho W/\rho_s h_a$, with $U_c = L/\tau$ being the characteristic velocity. The hydrodynamic performance of the plate is characterized by the dimensionless period-averaged thrust $\mathcal{F}$, power $\mathcal{P}$ and efficiency $\eta = \mathcal{F}/\mathcal{P}$, where the first two parameters are expressed in terms of the characteristic force $\frac{1}{2}\rho WLU_c^2$ and the characteristic power $\frac{1}{2}\rho WLU_c^3$. The thrust is computed by integrating the local hydrodynamic force in the x-direction acting on the surface of the plate. The overall propulsor length is set to $L = 50$ with $L_a = L_p = 0.5L$ and $\mathcal{A}_R = 2.5$. Unless specified otherwise we use the tapering ratio $b = 5$. We set the dimensionless bending moment $M_0 = 0.1$. We also set the fluid density $\rho = 1$, fluid viscosity $\mu = 1.25 \times 10^{-3}$ and oscillation period $\tau = 2000$, leading to $Re = 2000$ and $\chi = 5$. The fine and coarse fluid grids, respectively, measure $4L \times 3L \times 3L$ and $8L \times 6L \times 8L$, with respective spacing $\Delta_f = 1$ and $\Delta_c = 2$. The plate is discretized with 21 FD nodes in the length and 11 FD nodes in the width, resulting in $\Delta_x = 2.381$ and $\Delta_y = 1.82$. To ensure that the flow reaches a steady state, simulations are performed for 40 periods of plate oscillations. Note that all dimensional values are given in LBM units.

4. Results and discussion

4.1. *Acoustic black hole*

Mironov (1988) showed that, for tapered beams of finite length with thickness smoothly decreasing as $h : x \longmapsto \varepsilon x^n, n \in \mathbb{N}^*$, the wavenumber goes to infinity. This suggests that when flexural waves propagate along an elastic plate with a thickness gradually decreasing to zero, they slow down and increase in amplitude. Since the wave velocity decreases to zero as the thickness vanishes, flexural waves propagating along the plates never reach the plate end and, therefore, do not reflect. Note that, in this system, the lack of wave reflection is solely due to the wave's inability to reach the tapered end in a finite time and

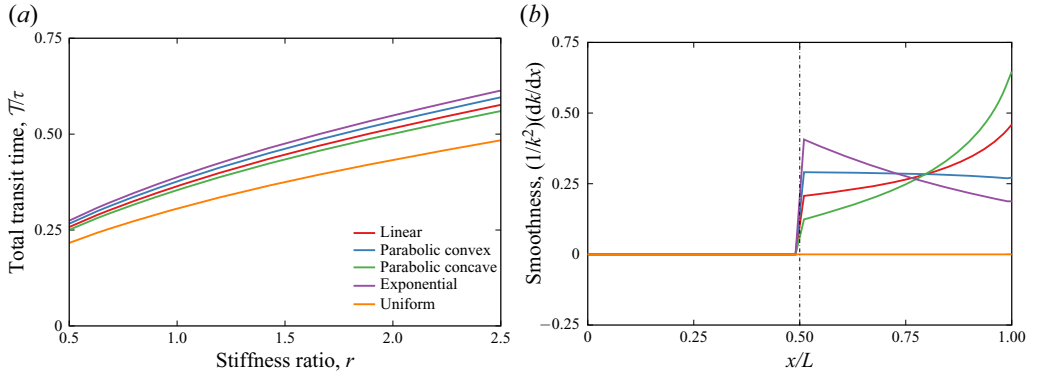

Figure 3. (*a*) Total transit time and (*b*) smoothness criterion for propulsors with passive attachments at resonance $r = 1$.

is not related to the absorption or damping of the wave. This suppression of flexural wave reflection results in a region where waves are trapped that is referred to as an ABH. Thus, ABH prevents the wave reflection resulting in the formation of travelling waves and the suppression of standing waves.

In practice, manufacturing a plate with a zero-thickness tip is not possible due to physical and structural limitations. When the plate tip thickness is not zero, reflections occur at the tip, substantially reducing the ABH effect (Mironov 1988; Pelat *et al.* 2020). With a tapering ratio $b = 5$, the transit time $\mathcal{T} = \int_0^L \mathrm{d}x/[2(E\omega^2/12\rho)^{1/4}\sqrt{h(x)}]$ increases by approximately 20 %–25 % compared with a plate with uniform thickness (figure 3*a*).

The ABH theory uses the regularity condition on the thickness, namely the Wentzel–Kramers–Brillouin–Liouville–Green condition (Liouville 1836; Green 1838; Brillouin 1926; Kramers 1926; Wentzel 1926), that postulates that the local wavenumber varies slowly over the wavelength $(1/k^2)(\mathrm{d}k/\mathrm{d}x) \ll 1$, where k is the wavenumber. This smoothness criterion is shown in figure 3(*b*) for the tapering shapes considered in this work. The interface between the uniform plate and the tapered attachment displays a jump in smoothness since the thickness is not differentiable at this point. Furthermore, steeper attachment shapes lead to less smooth transitions between the active and passive sections. The smoothness discontinuity can lead to wave reflections at the interface between the active section and the attachment, thereby diminishing the ABH effect and the formation of travelling waves. Thus, the smoothness needs to be minimized to maximize $\mathcal{T}$.

4.2. *Frequency response*

Figure 4 shows the Bode diagram for resonance oscillations of propulsors with different attachments with the tapering ratio $b = 5$. The solid symbols represent the response at the end of the active section, whereas the empty symbols show the response at the tip of the attachment. For all attachments, the root-mean-square (r.m.s.) velocity at the end of the active section shows a resonance maximum at $r = 1$ (figure 4*a*). The tip of the tapered sections displays a similar velocity dependence with the exception of the exponential attachment that has velocity continuously increasing with the frequency ratio r. Furthermore, we find that the 'steeper' tapering shapes result in higher tip velocities for the entire range of considered frequency ratios. For instance, at resonance the exponential tapering nearly doubles the tip velocity compared with the uniform plate. The enhancement of the tip velocity is even more significant for post-resonance frequencies.

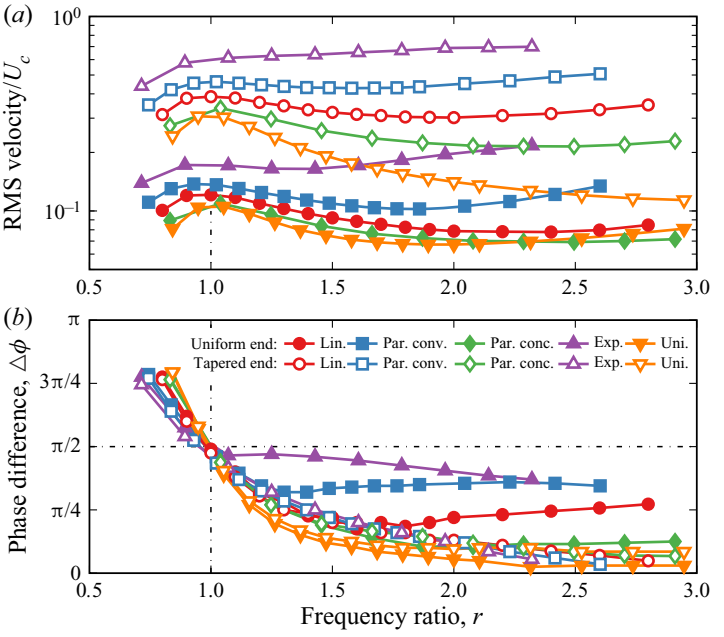

Figure 4. (*a*) The r.m.s. velocity and (*b*) phase difference of the internally actuated plate with several tapered passive attachments. The solid and empty symbols show the values for the ends of the tapered and uniform sections, respectively.

While the velocity of the uniform plate rapidly decreases for $r > 1$, the exponential tapering leads to a velocity increase. Moreover, the parabolic concave and linear tapered attachments display a velocity increase for $r > 2$. This is in contrast to the uniform plate attachment for which the velocity steadily decreases post-resonance with increasing r. Thus, our results for tapered attachments indicate that the tip velocity increases with increasing 'steepness' of the attachment and the high tip velocity is maintained for a wide range of frequency ratios.

At resonance $r = 1$, the phase difference $\Delta\phi = \pi/2$ and approaches asymptotically either 0 or π away from the resonance, with the slope being a function of the overall damping (figure 4*b*). Note that $\Delta\phi$ is defined as the phase difference between the input signal and the tip velocity. For the tapered attachment tip shown by the empty symbols, $\Delta\phi$ overlaps for all tapering shapes. Conversely, $\Delta\phi$ at the interface between the uniform and tapered sections, shown by the solid symbols, deviates from the uniform plate for $r > 1$. The steeper the tapering the earlier the deviation occurs.

4.3. *Bending pattern*

In figure 5(*a*), we show the bending pattern of the internally actuated plate with a uniform attachment actuated at resonance. The reflection at the attachment tip creates a standing wave characterized by in phase oscillations along the entire propulsor length. As shown in figure 5(*b*), the propulsor with an exponential attachment yields noticeably different bending patterns. Although the plate propulsor is actuated at resonance, the dynamic response combines travelling and standing waves. Due to the ABH effect, the tapered attachment impedes waves from reflecting at the tip, and thus, its bending pattern is characterized by a mix of standing and travelling waves.

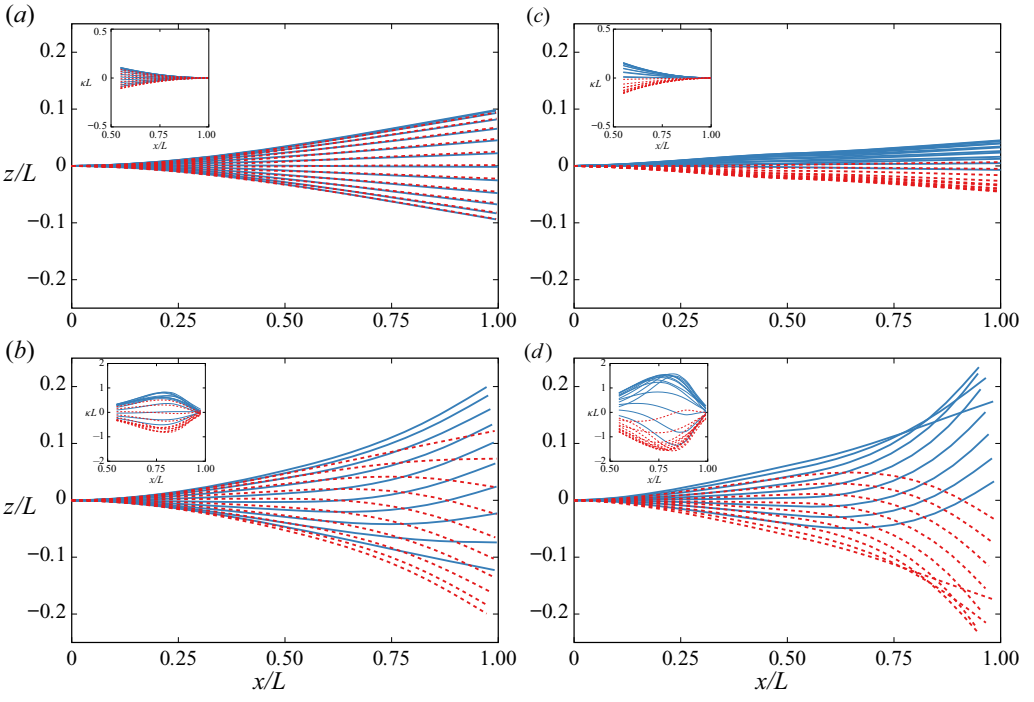

Figure 5. Bending patterns of propulsors at resonance $r = 1$ with (a) uniform attachment and (b) exponential attachment. Bending patterns of propulsors off resonance $r = 2$ with (c) uniform attachment and (d) exponential attachment. The insets show the attachment curvature. The solid blue lines correspond to $0 < t/\tau \leq 0.5$, while the dashed red lines correspond to $0.5 < t/\tau \leq 1$. Also see supplementary movie 1 available at https://doi.org/10.1017/jfm.2022.470.

In the insets in figures 5(a) and 5(b), we plot the curvature profiles $\kappa(x) = z''(x)/[1 + z'^2(x)]^{3/2}$ in the respective attachments at $r = 1$. The curvature pattern of the uniform attachment is typical for a passive plate with a monotonic envelope and a vanishing curvature at the free end. Conversely, the curvature of the exponentially tapered attachment displays a local maximum around $x/L \simeq 0.8$. Moreover, the maximum curvature amplitude is approximately six times that of the uniform attachment.

Off-resonance bending patterns at $r = 2$ for propulsors with uniform and exponential attachments are shown in figures 5(c) and 5(d), respectively. The bending patterns are characteristic of off-resonance oscillations with non-overlapping bending profiles for the up and down strokes, indicative of a combination of travelling and standing waves. The exponential attachment yields an approximately four times greater maximum tip displacement compared with the uniform attachment. Furthermore, the tip displacement of the exponential attachment at $r = 2$ exceeds its tip displacement at resonance at $r = 1$.

The tapering shape of the attachment significantly impacts the form of the oscillation envelope as measured by the curvature in the insets in figures 5(c) and 5(d). For the uniform attachment, the maximum curvature gradually decreases with x with a maximum $\kappa_{max}L \simeq 0.18$ at $x/L = 0.5$, while the exponential attachment displays a maximum $\kappa_{max}L \simeq 1.5$ at $x/L \simeq 0.8$. Due to the low bending stiffness at the tip, the same internal moment input leads to a greater curvature and, therefore, deformation of the tapered attachment compared with the uniform attachment.

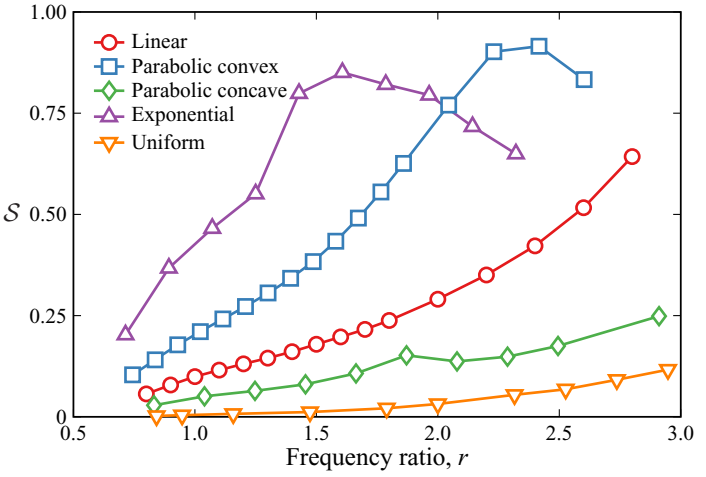

Figure 6. Travelling-to-standing wave ratio $\mathcal{S}$ as a function of the frequency ratio r for internally actuated plate propulsors with different attachments.

4.4. *Travelling-to-standing wave ratio*

Consider a travelling wave $u_t(x, t) = A_t \cos kx \cos \omega t + A_t \sin kx \sin \omega t$ and a standing wave $u_s(x, t) = A_s \cos kx \cos \omega t$. A general wave resulting from the superposition of a standing and travelling wave is then given by $\hat{u}(x, t) = \cos(kx) \cos(\omega t) \pm \mathcal{S} \sin(kx) \sin(\omega t)$, where $\mathcal{S} = A_t/(A_t + A_s)$ is the travelling-to-standing wave ratio and $\hat{u}$ is amplitude-normalized velocity. The magnitude of $\mathcal{S}$ quantifies the fraction of the travelling wave in the superposition. The ratio is zero when the oscillations represent a standing wave and unity for a travelling wave. We use $\mathcal{S}$ to quantify the combination of travelling and standing waves resulting from the addition of a tapered attachment. Evaluation of $\mathcal{S}$ is based on the fitting a Hilbert transform onto an ellipse in the complex plane (Minikes *et al.* 2005).

Figure 6 shows the dependence of $\mathcal{S}$ on the frequency ratio r. We find that steeper tapering leads to a greater $\mathcal{S}$. Furthermore, as the frequency ratio increases, $\mathcal{S}$ increases with the rate depending on the tapering shape. For the exponential and parabolic convex shapes, $\mathcal{S}$ reaches maxima for $r \simeq 1.6$ and $r \simeq 2.4$, respectively. Past these frequencies, $\mathcal{S}$ decreases for both tapering shapes. We speculate that similar maxima exist for less 'steep' tapering shapes at frequencies that exceed those considered in our simulations. Although it is less 'steep', the parabolic convex attachment yields an approximately 10 % higher $\mathcal{S}$ than the exponential attachment. Similarly, $\mathcal{S}$ due to linear tapering increases steadily and nearly surpasses the exponential $\mathcal{S}$ for sufficiently large r. These observations indicate that the sharper tapering causes a faster increase in $\mathcal{S}$ with r, however, the maximum value is not directly defined by the tapering steepness. This can be related to a smoother transition at the interface between the active and passive segments for the propulsor with the parabolic convex attachment compared with the exponential attachment (figure 3*b*). A sharp change at the interface between active and passive segments can lead to spurious modes and reflections affecting the formation of travelling waves. Overall, the significant increase in $\mathcal{S}$ shows that tapered attachments with non-vanishing tip thickness are an effective solution to maintaining travelling waves in plate propulsors of finite length.

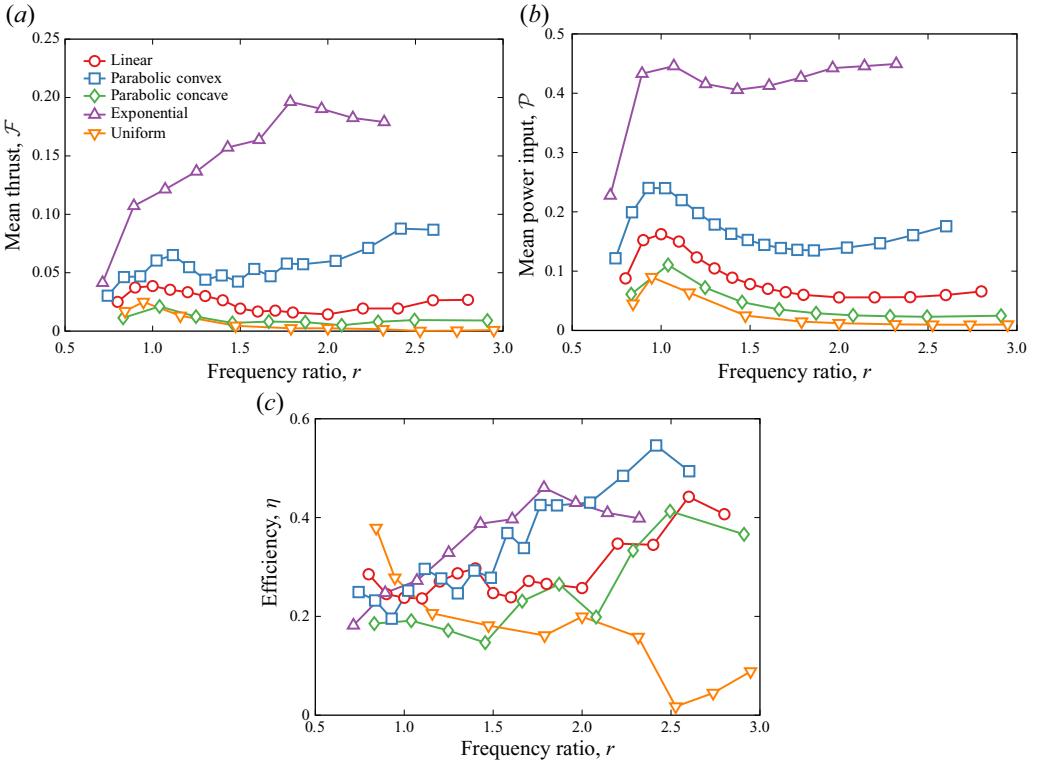

Figure 7. (*a*) Thrust, (*b*) power and (*c*) efficiency as a function of the frequency ratio r for internally actuated plates with different tapered attachments.

4.5. *Hydrodynamic performance*

In figure 7(*a*), we plot the dimensionless thrust $\mathcal{F}$ as a function of the frequency ratio r for propulsors with different passive attachments. For the uniform attachment, the thrust is maximized at resonance and rapidly decreases off resonance, which correlates with the plate r.m.s. velocity (figure 4). By comparing the thrust for different attachments at $r = 1$, our results demonstrate that the attachments with steeper tapering generate more thrust, with the maximum $\mathcal{F}$ yielded by the exponential attachment. The parabolic concave and linear tapered attachments perform similarly to the uniform attachment. The thrust produced by the exponential and parabolic convex attachments noticeably exceeds the $\mathcal{F}$ generated by the other attachments. In the case of the exponential attachment, the local maximum thrust does not occur near the first resonance frequency; rather, the thrust steadily increases with the frequency ratio until it peaks at $r \simeq 1.8$. For the parabolic convex attachment, the maximum thrust is generated at $r \simeq 2.4$. Note that the maximum thrust generated by the propulsor with the exponential attachment is nearly 8 times greater than the maximum thrust of the propulsor with the uniform thickness. Thus, thickness tapering can drastically enhance the hydrodynamic thrust.

In figure 7(*b*), we plot the dimensionless power input $\mathcal{P}$ as a function of r. We find that tapered attachments require higher power than the attachment with uniform thickness. For instance, the exponential attachment requires more than four times the power input of the uniform attachment at $r = 1$. Indeed, the tapered attachment results in a higher tip displacement and a greater deformation envelope (figures 5). The larger deformation

envelope leads to an increased fluid displacement and viscous dissipation magnifying the power consumption.

In figure 7(*c*), we plot the propulsor efficiency η as a function of r. In the case of the uniform passive attachment, the efficiency decreases until it reaches a local minimum at $r \simeq 1.7$. The efficiency then slightly increases to a local maximum at $r \simeq 2$ followed by a steep decrease. In other words, in the case of the uniform attachment, the actuation frequency has to be precisely tuned to achieve the optimal efficiency. For the tapered attachments, the efficiency is near the minimum at the resonance, with the magnitude close to that of the uniform propulsor. However, the tapered attachments outperform the uniform attachment for driving frequencies past the resonance. For instance, the parabolic convex attachment yields $\eta \simeq 0.55$ for $r = 2.4$, which is nearly 1.4 times greater than the maximum efficiency of the uniform attachment. Interestingly, the parabolic convex attachment, while it does not have the 'steepest' tapering, outperforms the exponential attachment. This is correlated with the higher values of $\mathcal{S}$ for the parabolic convex attachment (figure 6), indicating that travelling waves enhance the propulsor hydrodynamic efficiency.

4.6. *Scaling metrics*

In figure 8(*a*), we plot the relationship between the dimensionless thrust $\mathcal{F}$ and the dimensionless tip displacement d/L for attachments with different shapes and two tapering ratios. The colour of the markers indicates the magnitude of the frequency ratio r. Our results show that the thrust scales with the tip displacement as $\mathcal{F} \sim d^3$, independently of the tapering shape and the tapering ratio b (left inset in figure 8*a*). We find that steeper tapering shapes enable greater tip displacement, which ultimately, leads to higher thrust. In other words, tapered attachments can be used to maximize the tip displacement for a wide range of actuation frequencies, which in turn enhances the hydrodynamic thrust. The dependence of the thrust on tip displacement is consistent with the literature data for uniform propulsors (Lighthill 1970; Dewey *et al.* 2013; Floryan *et al.* 2017; Ayancik *et al.* 2019; Lagopoulos, Weymouth & Ganapathisubramani 2019). Furthermore, we find that our simulation results for $\mathcal{F}$ are in good agreement with the scaling derived by Gazzola, Argentina & Mahadevan (2014) and confirmed experimentally by Gibouin *et al.* (2018) (right inset in figure 8*a*). This result indicates that our simulations follow the same scaling behaviour that is universal for aquatic animals at the limit of large *Re*.

Previous studies indicate that the power input is proportional to the relative motion between the fluid and the oscillating plate leading to viscous dissipation (Yeh & Alexeev 2014; Demirer, Oshinowo & Alexeev 2021*a*; Demirer *et al.* 2021*b*). To estimate this power metric, we evaluate the maximum displacement area of the propulsor $\mathcal{A} = \max_t(1/L^2) \int_0^L w(x, t)\,\mathrm{d}x$, where w is the displacement of the plate along the centreline. In figure 8(*b*), we plot the mean dimensionless power $\mathcal{P}$ as a function of $\mathcal{A}$ for propulsors with different attachments and b. We find that all data collapse on a master curve, indicating a direct relationship between the power and the displacement area such that $\mathcal{P} \sim \mathcal{A}^3$ (inset in figure 8*b*). We conclude that minimizing the maximum displacement area decreases the power input.

The propulsor efficiency η is defined as the ratio between the dimensionless thrust $\mathcal{F}$ and the dimensionless power $\mathcal{P}$ that are, respectively, proportional to d and $\mathcal{A}$. In figure 9(*a*), we plot η as a function of $\mathcal{A}L/d$. The colour of the markers indicates the magnitude of $\mathcal{F}$. We find that the efficiency is correlated with $\mathcal{A}L/d$, and that a lower magnitude of this ratio leads to a higher efficiency. The low values of $\mathcal{A}L/d$, however, do not ensure

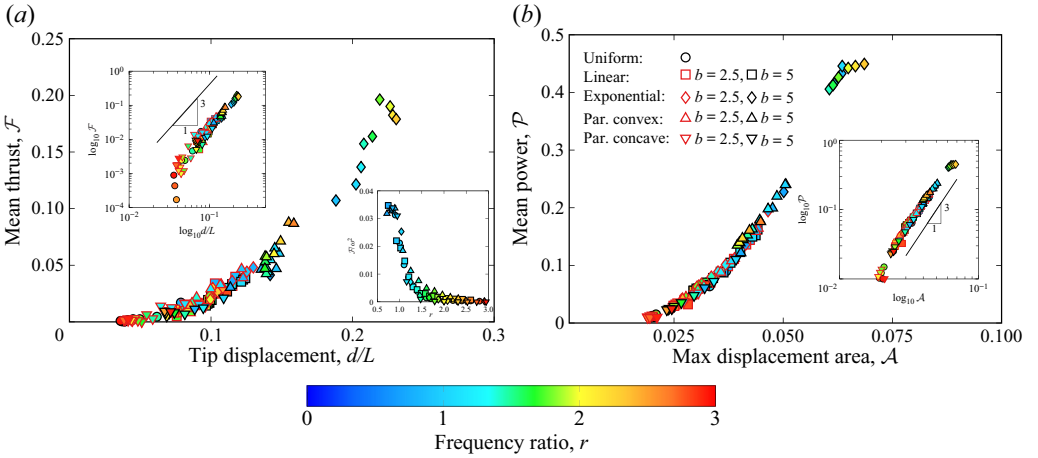

Figure 8. (*a*) Thrust as a function of tip displacement. (*b*) Power as a function of the dimensionless maximum displacement area. The data are for internally actuated propulsors with different passive attachments for $b = 2.5$ and $b = 5$.

high $\mathcal{F}$. In a relatively narrow band of $\mathcal{A}L/d$ between 14 and 15, $\mathcal{F}$ for different propulsors ranges from 0.025 to 0.2. Indeed, a low $\mathcal{A}L/d$ can correspond to different values of d. Whereas larger d results in significant $\mathcal{F}$, low d produces weak propulsion even when the bending pattern is characterized by a sufficiently low $\mathcal{A}$ to yield high η.

Since the hydrodynamic efficiency is associated with travelling waves (Cui *et al.* 2018), in figure 9(*b*) we plot η as a function of the travelling-to-standing wave ratio $\mathcal{S}$ with the marker colour indicating $\mathcal{F}$. At low $\mathcal{S}$, we find a significant spread of the efficiency without a clear trend that includes propulsors with tapered and uniform attachments. For high values of $\mathcal{S}$, there is a direct correlation between the high propulsion efficiency and $\mathcal{S}$ such that $\eta \sim \mathcal{S}^{0.4}$ (inset in figure 9*b*). Moreover, high $\mathcal{S}$ yields high thrust output. Indeed, for $\mathcal{S} > 0.5$ the thrust is in the range between 0.05 and 0.2.

When we plot $\mathcal{S}$ as a function of the ratio $\mathcal{A}L/d$ (figure 9*c*), we find that the data from different simulations collapse into a single curve where at the lower spectrum of $\mathcal{A}L/d$ the higher values of $\mathcal{S}$ yield greater thrust. Thus, larger values of $\mathcal{S}$ result in oscillations with lower $\mathcal{A}L/d$ and, at the same time, higher d yielding greater $\mathcal{F}$ (figure 8*a*). Since large $\mathcal{S}$ are associated with the ABH effect at the tapered attachments (figure 6), we conclude that propulsors with such attachments exhibit the travelling wave propulsion leading to high η and $\mathcal{F}$.

4.7. *Flow patterns*

As the plate deforms, the relative motion between the plate and the fluid results in vorticity that is the most significant along the trailing edge and side edges. The vorticity is associated with hydrodynamic propulsion and dissipation (Anderson *et al.* 1998; Nauen & Lauder 2002; Alben 2009; Michelin & Llewellyn Smith 2009; Yeh & Alexeev 2014; Paraz, Schouveiler & Eloy 2016; Yeh & Alexeev 2016*b*). Figures 10 and 11 show representative contours of Q-criterion (the second invariant of the velocity gradient tensor) coloured by the magnitude of the y-component of the vorticity for propulsors with the uniform and exponential attachments, respectively. The flow structures in these figures are typical of oscillating plate propulsors (Facci & Porfiri 2013; Demirer *et al.* 2021*b*) with the formation of trailing edge vortices (TEVs) and side edge vortices (SEVs). While the TEVs generate thrust by forming a jet in the wake, the SEVs are typically detrimental to the propulsor

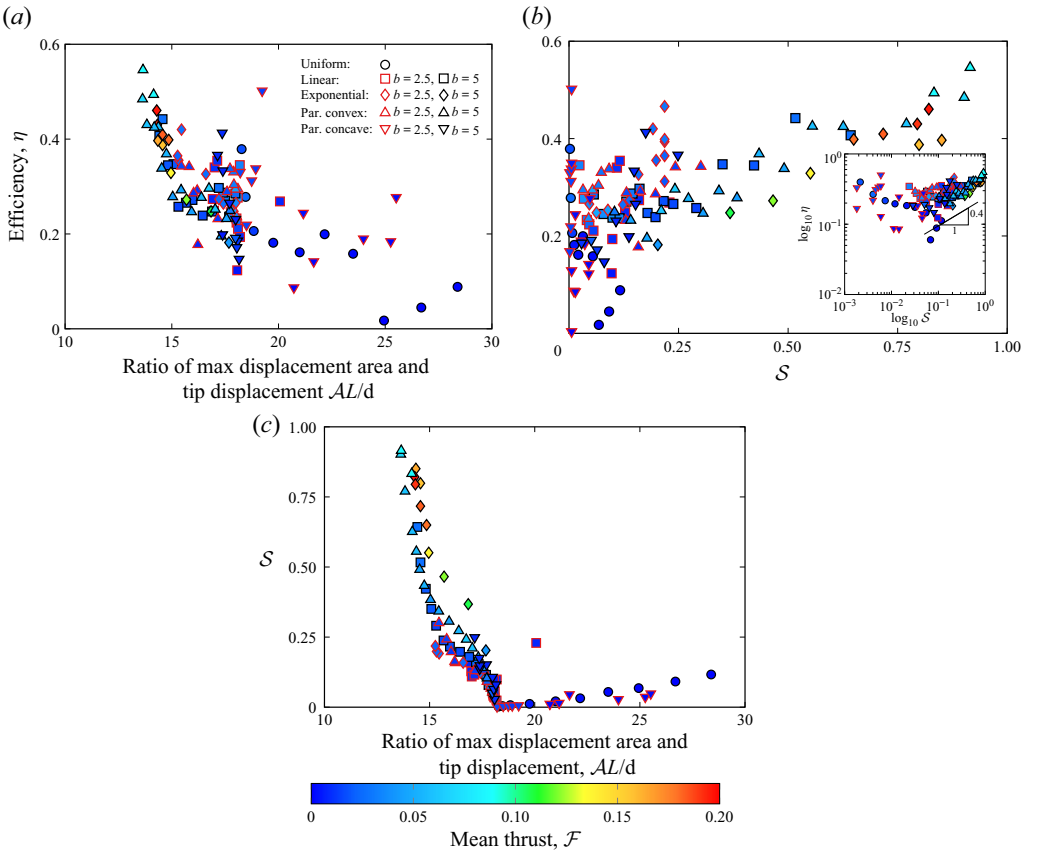

Figure 9. Efficiency as a function of (*a*) the ratio between the maximum displacement area and tip displacement and (*b*) the travelling-to-standing wave ratio. (*c*) Travelling-to-standing wave ratio as a function of the ratio between the maximum displacement area and tip displacement. The data are for internally propulsors with different passive attachments for $b = 2.5$ and $b = 5$.

hydrodynamic efficiency by dissipating energy without creating propulsion. Comparing the two attachments at resonance $r = 1$ (figures 10(*a*) and 11(*a*)), the exponential attachment produces a greater amount of vorticity that can be attributed to an increased amplitude of the trailing edge displacement.

The difference between the vorticity fields of the two propulsors is even more dramatic at the post resonance frequency $r = 2$ (figures 10(*b*) and 11(*b*)). At $r = 2$ the propulsor with the uniform attachment exhibits significantly lower deformation than at resonance, yielding a relatively low amount of vorticity generated by the propulsor. On the other hand, the deformation amplitude of the exponential propulsor at $r = 2$ exceeds the amplitude at resonance, and so does the vorticity that significantly exceeds that of the propulsor with the uniform attachment at $r = 2$. This explains the greater hydrodynamic performance of the propulsor with the tapered exponential attachment that takes place not only at resonance, but also for post-resonance actuation frequencies.

To examine the impact of travelling waves on the propulsor hydrodynamics and the emerging flow patterns, we compare two propulsor configurations with similar tip displacement d and displacement area $\mathcal{A}$, but different magnitude of travelling-to-standing wave ratio $\mathcal{S}$. Specifically, in figures 12(*a*) and 12(*b*), we show propulsors with the parabolic convex attachments at $r = 1.2$ and $r = 2.4$, respectively. The parameters of these

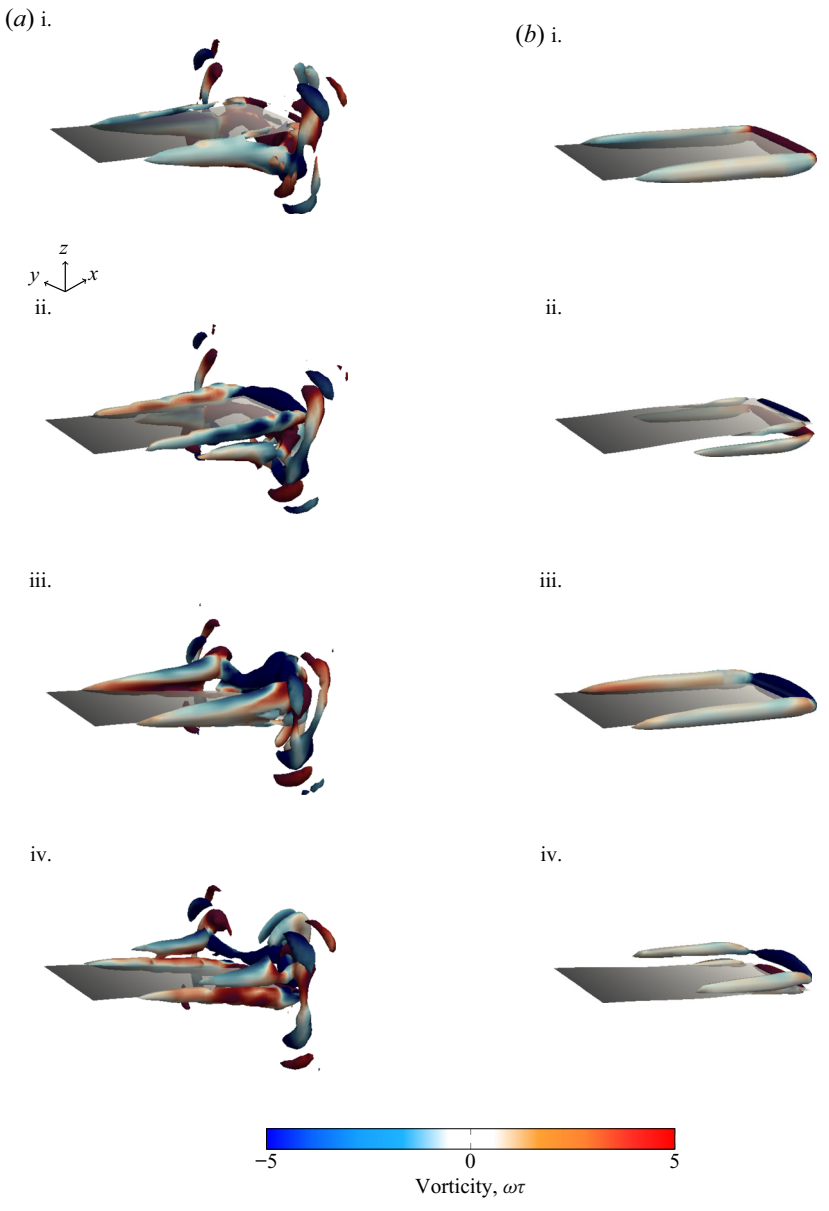

Figure 10. Snapshots of normalized $\mathcal{Q}$-criterion contours ($\mathcal{Q}\tau^2 = 5$) coloured by y-component of the vorticity for the propulsors with the uniform attachment (a) at resonance $r = 1$ and (b) off resonance $r = 2$. The snapshots are for (i) $t/\tau = 0$, (ii) $t/\tau = 0.25$, (iii) $t/\tau = 0.5$ and (iv) $t/\tau = 0.75$. See supplementary movie 2.

two cases are presented in table 1. At the lower frequency ratio, the plate oscillations are mostly a standing wave ($\mathcal{S} \simeq 0.2$), whereas at the higher frequency ratio, the plate exhibits travelling waves propagating along the propulsor ($\mathcal{S} \simeq 0.9$). The oscillations with travelling waves produce higher thrust with lower input power. As a result, the oscillations at $r = 2.4$ are twice as efficient than at $r = 1.2$. Figure 12 shows that both these configurations generate similar levels of vorticity with dominant TEVs and SEVs, although oscillations at $r = 2.4$ produce somewhat lower mean enstrophy $\mathcal{E} = \boldsymbol{\omega} \times \boldsymbol{\omega}\tau^2$

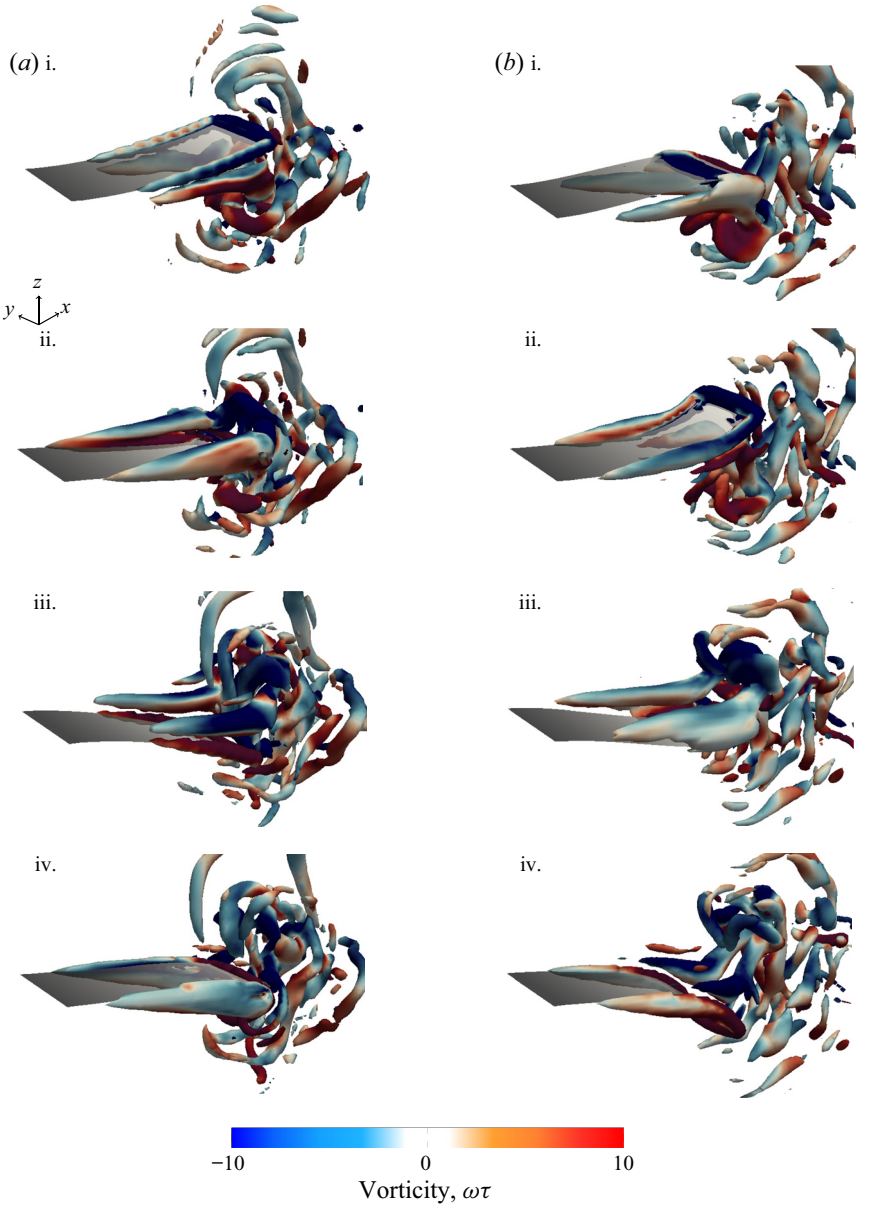

Figure 11. Snapshots of normalized $\mathcal{Q}$-criterion contours ($\mathcal{Q}\tau^2 = 10$) coloured by y-component of the vorticity for the propulsors with the exponential attachment (a) at resonance $r = 1$ and (b) off resonance $r = 2$. The snapshots are for (i) $t/\tau = 0$, (ii) $t/\tau = 0.25$, (iii) $t/\tau = 0.5$ and (iv) $t/\tau = 0.75$. See supplementary movie 3.

that quantifies the intensity of viscous dissipation by the plate (table 1). We find that the dynamics of the vortical fields is noticeably different for the oscillations characterized by standing and travelling waves. For standing wave oscillations at $r = 1.2$, there are relatively weak interactions between TEVs and SEVs. On the other hand, for travelling wave oscillations at $r = 2.4$, the waves propagating along the propulsor length transport SEVs towards the trailing edge where SEVs interact with TEVs.

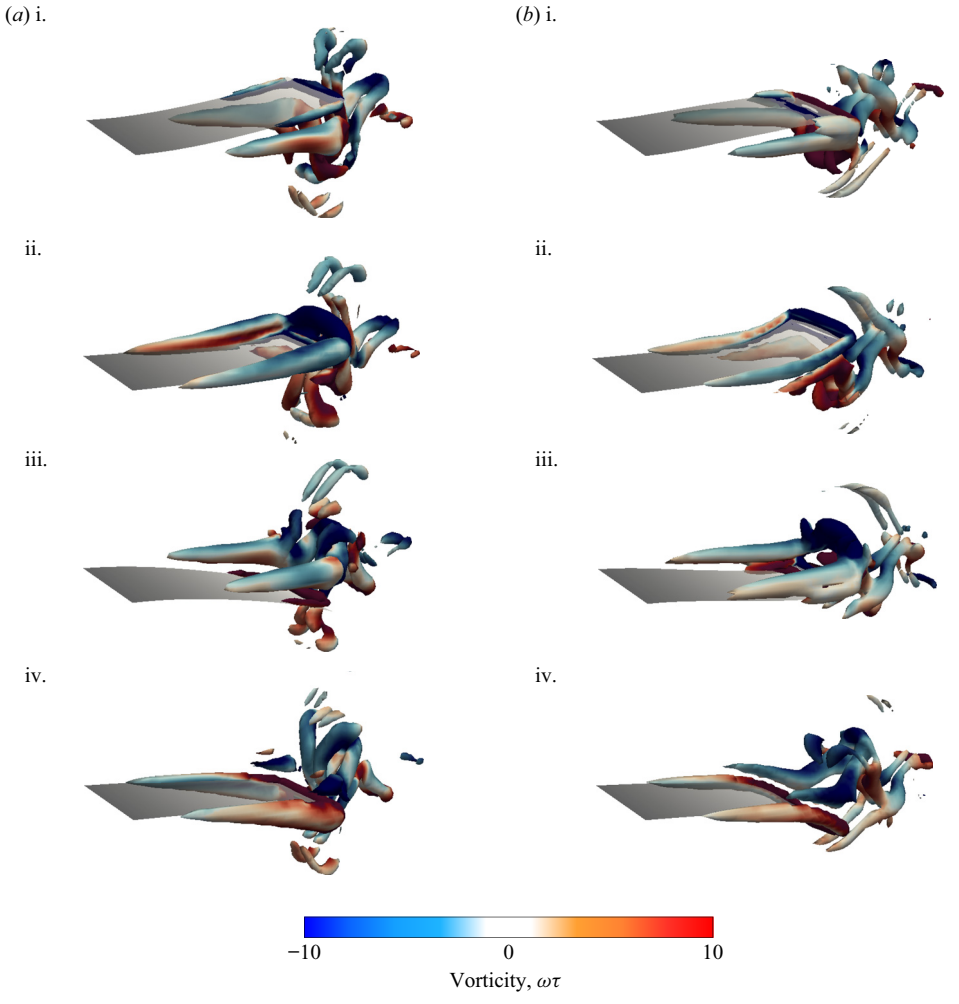

Figure 12. Snapshots of normalized $\mathcal{Q}$-criterion contours ($\mathcal{Q}\tau^2 = 10$) coloured by y-component of the vorticity for the propulsors with the parabolic convex attachment (a) at $r = 1.2$ and (b) at $r = 2.4$. The snapshots are for (i) $t/\tau = 0$, (ii) $t/\tau = 0.25$, (iii) $t/\tau = 0.5$ and (iv) $t/\tau = 0.75$. See supplemental movie 4.

In figures 13(a) and 13(b), we show the out-of-plane component of the vorticity ω_y generated by the parabolic convex propulsors at $r = 1.2$ and $r = 2.4$, respectively. The vorticity is shown at the mid-plane of the plates. The relative motion between the plate and the flow results in vortices generated about the midchord and shed towards the tip. The alternating clockwise and counter-clockwise shedding structure is characteristic of a reverse von Kármán vortex street (Anderson *et al.* 1998; Von Ellenrieder, Parker & Soria 2003; Lentink *et al.* 2008). The rotation of the vortices induces an increase in the streamwise component of the momentum, and thus enhances the propulsion. The downstream vortex structures of the two oscillation regimes are distinctively different. For the travelling wave oscillations at $r = 2.4$, a bifurcating wake develops downstream of the propulsor due to greater vortex intensity. As vortices shed streamwise, they stretch and, due to significant cross-stream velocity, break into smaller vortices moving orthogonal to the streamwise direction forming a bifurcating wake.

Frequency ratio, r	1.2	2.4
Thrust, $\mathcal{F}$	0.0548	0.0877
Power, $\mathcal{P}$	0.198	0.161
Efficiency, η	0.277	0.546
Max tip disp., d/L	0.142	0.155
Max disp. area, $\mathcal{A}$	0.0465	0.0423
Enstrophy, $\mathcal{E}$	0.809	0.724

Table 1. Hydrodynamic parameters of the parabolic convex attachment at $r = 1.2$ and $r = 2.4$.

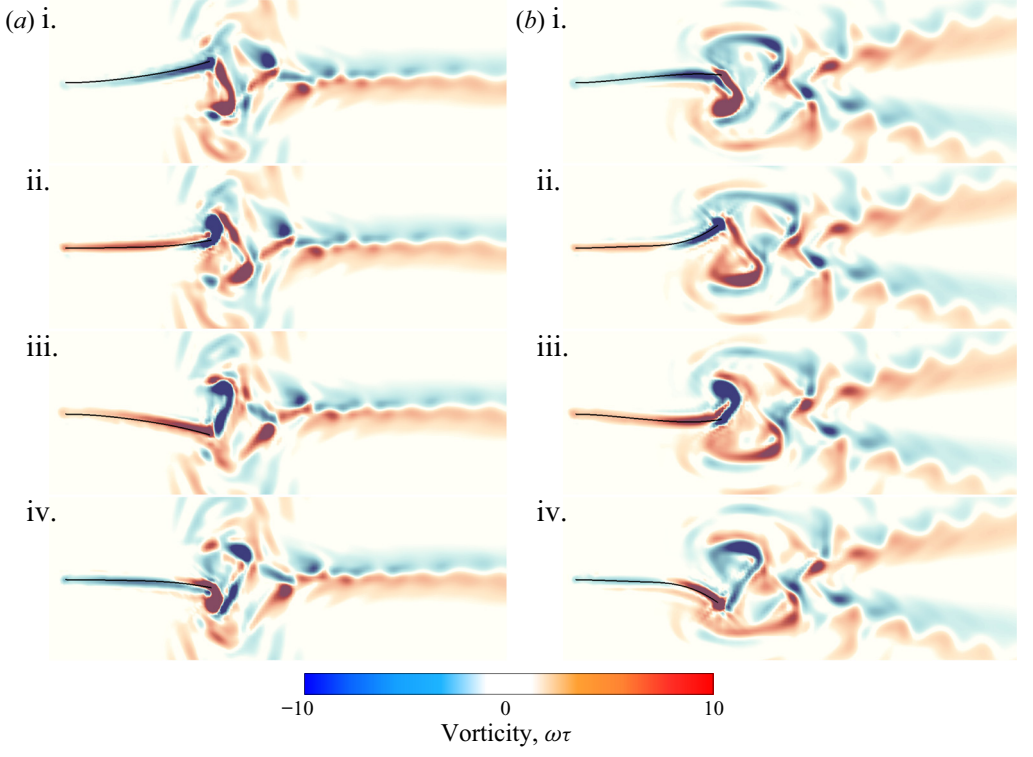

Figure 13. Snapshots of normalized vorticity field at (*a*) $r = 1.2$ and (*b*) $r = 2.4$ for the parabolic convex attachment. The snapshots are for (i) $t/\tau = 0$, (ii) $t/\tau = 0.25$, (iii) $t/\tau = 0.5$ and (iv) $t/\tau = 0.75$. See supplemental movie 5.

The bifurcating wake structure is further confirmed in figure 14(*a*,*b*), where we plot the time-averaged velocity field for the propulsor with parabolic convex attachment actuated at $r = 1.2$ and $r = 2.4$. The figure reveals a narrowing jet in the streamwise direction for $r = 1.2$, whereas at higher $r = 2.4$ the propulsor oscillations result in a pair of narrowing jets at an acute angle with the streamwise direction. Travelling waves cause a faster mean flow speed along the propulsor, enhancing propulsor performance (figure 14*c*). This flow structure is characteristic of undulating elastic propulsors (Borazjani & Sotiropoulos 2008, 2009; Godoy-Diana *et al.* 2009) and fish swimming (Tytell & Lauder 2004; Hultmark, Leftwich & Smits 2007; Wu 2011), where bifurcating wakes emerge at higher Strouhal numbers *St* and are associated with enhanced propulsion efficiency.

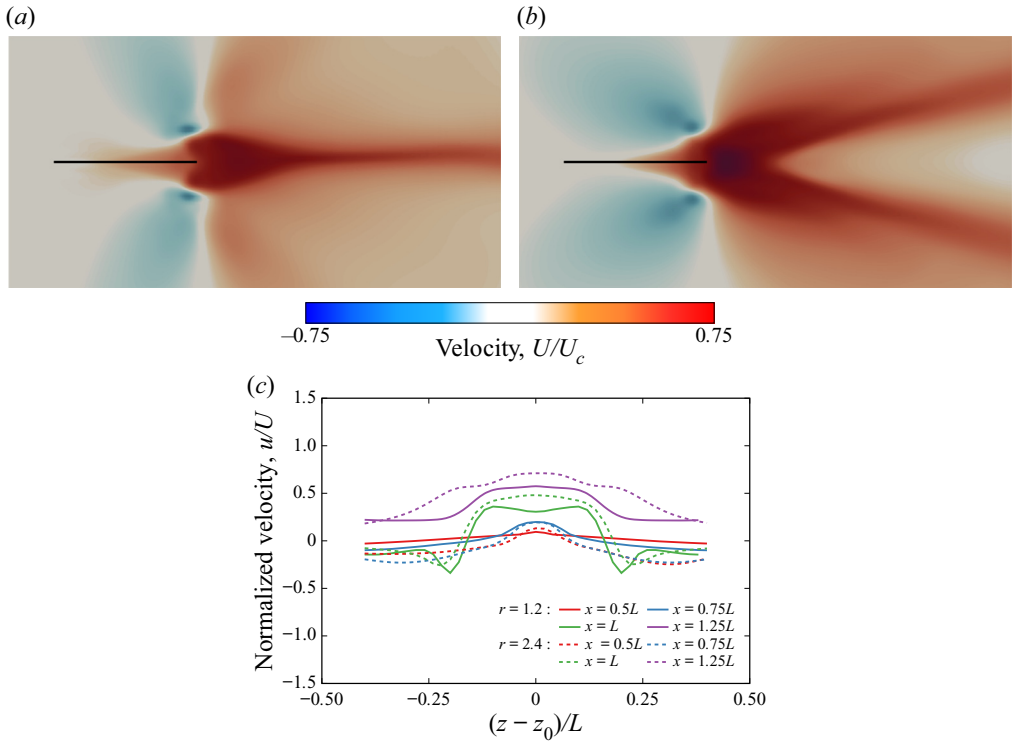

Figure 14. Time-averaged velocity field at (*a*) $r = 1.2$ and (*b*) $r = 2.4$ for the parabolic convex attachment. (*c*) Normalized x-component of the period-averaged velocity profiles at various positions along the plate and wake for $r = 1.2$ and $r = 2.4$.

5. Summary

We use three-dimensional computer simulations to probe the hydrodynamic performance of bio-mimetic elastic propulsors with tapered thickness. The propulsors are composed of an active section at the base inducing the propulsor periodic oscillations in an incompressible Newtonian fluid, and a passive attachment with tapered thickness. The tapering aims to create the ABH effect leading to a wave speed decrease towards the propulsor trailing edge, thereby suppressing the flexural wave reflection and promoting the formation of travelling waves. As a result, the propulsors with ABH exhibit beating patterns that feature travelling flexural waves propagating along the propulsor length. By altering the propulsor thickness profile, the strength of ABH can be regulated yielding propulsors with different ratios between the travelling and standing waves in their beating patterns. We find that the travelling-to-standing wave ratio is approximately zero for uniformly thick propulsors, indicating that the propulsor oscillations are standing flexural waves, whereas for exponential and parabolic convex tapered propulsors, the value of the ratio approaches unity, indicating the dominance of travelling waves in the beating patterns. We directly evaluate and compare the hydrodynamic performance of propulsors with beating patterns that exhibit different levels of travelling-to-standing wave ratios.

Our simulations reveal that tapered propulsors with ABH significantly outperform propulsors with uniform thickness in terms of the hydrodynamic thrust and efficiency for a broad range of actuation frequencies, including resonance and off-resonance oscillations.

Tapering increases the magnitude of the tip displacement compared with uniform propulsors, thereby leading to greater thrust that is directly proportional to the tip displacement magnitude. Furthermore, tapered propulsors with ABH leading to high travelling-to-standing wave ratios demonstrate a superior efficiency defined as the ratio of the dimensionless thrust and power. We show that the input power is proportional to the amount of fluid displaced by an oscillating propulsor. For uniform propulsors with standing wave oscillations, the frequency regimes leading to reduced input power also result in the lower tip displacement magnitude and, therefore, weak thrust. Thus, for uniform propulsors there is a trade-off between high thrust and high efficiency. By contrast, travelling wave propulsion yields bending patterns with relatively low input power while maintaining a high tip displacement amplitude.

We examine the flow field and vortical structures generated by propulsors with standing and travelling waves and show that standing waves yield a reverse von Kármán vortex street, whereas travelling waves generate a bifurcating wake downstream of the propulsor. The travelling wave oscillations with bifurcating wake lead to significantly higher propulsion and efficiency than standing wave oscillations of comparable oscillation magnitude. We attribute this to the increased fluid transport by the travelling waves propagating along the propulsor length. Furthermore, travelling waves increase interactions among SEVs and TEVs by transporting SEVs towards the trailing edge. Whereas, for standing wave oscillations, SEVs do not participate in generating forward thrust, the interaction of SEVs with TEVs by travelling waves enhances the vorticity and, therefore, the momentum transfer facilitating propulsion, similar to the positive reinforcement observed for leading edge vortices (Lewin & Haj-Hariri 2003; Guglielmini & Blondeaux 2004). The unique ability of tapered propulsors with ABH to generate high thrust with high efficiency makes them excellent candidates for designing highly efficient bio-mimetic robotic swimmers.

Our results support the observations that the travelling wave-based anguilliform swimming of fishes such as eels and lampreys is beneficial for the efficient locomotion (Lighthill 1970; Borazjani & Sotiropoulos 2010). Our simulations offer an explanation for the better energetic performance reported for travelling wave-based swimming over standing wave-based swimming at lower Re (Tytell 2010; Tytell *et al.* 2010). On the other hand, we do not find an advantage of standing wave oscillations over travelling wave oscillations in generating propulsion thrust, suggesting that travelling waves are beneficial for thunniform swimming. We note that several aspects of our study can limit the extent to which our results can be applied to biological fish. Here, we explore swimming at $Re = 2000$, whereas thunniform and ostraciiform swimming are more typical for faster fish with higher Re (Lindsey 1978; Sfakiotakis, Lane & Davies 1999). We consider oscillations with a wavelength that is approximately twice longer than the propulsor length as typical for thunniform fish, whereas angulliform fish have a wavelength approximately half of the fish body length (Smits 2019). Furthermore, we consider propulsors with simplified rectangular geometry and disregard the hydrodynamic effects of the fish body. Finally, the form of fish swimming is tightly related to the fish physiology and, in particular, the muscle function (Webb 1994; Müller & Van Leeuwen 2006; Cohen & Boyle 2010), which makes a direct hydrodynamic comparison between different forms of fish swimming more challenging and points to the need for future studies using more elaborate models.

Supplementary movies. Supplementary movies are available at https://doi.org/10.1017/jfm.2022.470.

Acknowledgements. Stimulating discussions with Dr R. Godoy-Diana are gratefully acknowledged.

Funding. We thank the National Science Foundation (CBET-1705739) for financial support. The work used the Extreme Science and Engineering Discovery Environment (XSEDE) provided through Award TG-DMR180038.

Declaration of interests. The authors report no conflict of interest.

Author ORCIDs.
Ersan Demirer https://orcid.org/0000-0002-9710-6906;
Alexander Alexeev https://orcid.org/0000-0002-8285-0003.

References

Aiello, B.R., Hardy, A.R., Cherian, C., Olsen, A.M., Ahn, S.E., Hale, M.E. & Westneat, M.W. 2018 The relationship between pectoral fin ray stiffness and swimming behavior in labridae: insights into design, performance and ecology. *J. Expl Biol.* **221** (1), jeb163360.

Aiello, B.R., Westneat, M.W. & Hale, M.E. 2017 Mechanosensation is evolutionarily tuned to locomotor mechanics. *Proc. Natl Acad. Sci. USA* **114** (17), 4459–4464.

Alben, S. 2009 On the swimming of a flexible body in a vortex street. *J. Fluid Mech.* **635**, 27–45.

Alben, S., Madden, P.G. & Lauder, G.V. 2007 The mechanics of active fin-shape control in ray-finned fishes. *J. R. Soc. Interface* **4** (13), 243–256.

Alexeev, A. & Balazs, A.C. 2007 Designing smart systems to selectively entrap and burst microcapsules. *Soft Matt.* **3** (12), 1500–1505.

Alexeev, A., Verberg, R. & Balazs, A.C. 2005 Modeling the motion of microcapsules on compliant polymeric surfaces. *Macromolecules* **38** (24), 10244–10260.

Anderson, J.M., Streitlien, K., Barrett, D.S. & Triantafyllou, M.S. 1998 Oscillating foils of high propulsive efficiency. *J. Fluid Mech.* **360**, 41–72.

Ayancik, F., Zhong, Q., Quinn, D.B., Brandes, A., Bart-Smith, H. & Moored, K.W. 2019 Scaling laws for the propulsive performance of three-dimensional pitching propulsors. *J. Fluid Mech.* **871**, 1117–1138.

Borazjani, I. & Sotiropoulos, F. 2008 Numerical investigation of the hydrodynamics of carangiform swimming in the transitional and inertial flow regimes. *J. Expl Biol.* **211** (10), 1541–1558.

Borazjani, I. & Sotiropoulos, F. 2009 Numerical investigation of the hydrodynamics of anguilliform swimming in the transitional and inertial flow regimes. *J. Expl Biol.* **212** (4), 576–592.

Borazjani, I. & Sotiropoulos, F. 2010 On the role of form and kinematics on the hydrodynamics of self-propelled body/caudal fin swimming. *J. Expl Biol.* **213** (1), 89–107.

Bouzidi, M., Firdaouss, M. & Lallemand, P. 2001 Momentum transfer of a Boltzmann-Lattice fluid with boundaries. *Phys. Fluids* **13** (11), 3452–3459.

Bowtell, G. & Williams, T. 1991 Anguilliform body dynamics: modelling the interaction between muscle activation and body curvature. *Phil. Trans. R. Soc. Lond.* B **334** (1271), 385–390.

Bowyer, E.P. & Krylov, V.V. 2015 Experimental study of sound radiation by plates containing circular indentations of power-law profile. *Appl. Acoust.* **88**, 30–37.

Branscomb, J. & Alexeev, A. 2010 Designing ciliated surfaces that regulate deposition of solid particles. *Soft Matt.* **6** (17), 4066–4069.

Brillouin, L. 1926 La mécanique ondulatoire de Schrödinger; une méthode générale de résolution par approximations successives. *C. R. Hebd. Seances Acad. Sci.* **183**, 24–26.

Chun, B. & Ladd, A.J.C. 2007 Interpolated boundary condition for Lattice Boltzmann simulations of flows in narrow gaps. *Phys. Rev.* E **75**, 066705.

Cohen, N. & Boyle, J.H. 2010 Swimming at low Reynolds number: a beginners guide to undulatory locomotion. *Contemp. Phys.* **51** (2), 103–123.

Conlon, S.C., Fahnline, J.B. & Semperlotti, F. 2015 Numerical analysis of the vibroacoustic properties of plates with embedded grids of acoustic black holes. *J. Acoust. Soc. Am.* **137** (1), 447–457.

Cui, Z., Yang, Z., Shen, L. & Jiang, H.Z. 2018 Complex modal analysis of the movements of swimming fish propelled by body and/or caudal fin. *Wave Motion* **78**, 83–97.

Demirer, E., Oshinowo, O.A. & Alexeev, A. 2021*a* Efficient aquatic locomotion using elastic propulsors with hybrid actuation. *J. Fluid Mech.* **922**, A21.

Demirer, E., Wang, Y.-C., Erturk, A. & Alexeev, A. 2021*b* Effect of actuation method on hydrodynamics of elastic plates oscillating at resonance. *J. Fluid Mech.* **910**, A4.

DEWEY, P.A., BOSCHITSCH, B.M., MOORED, K.W., STONE, H.A. & SMITS, A.J. 2013 Scaling laws for the thrust production of flexible pitching panels. *J. Fluid Mech.* **732**, 29–46.

FACCI, A.L. & PORFIRI, M. 2013 Analysis of three-dimensional effects in oscillating cantilevers immersed in viscous fluids. *J. Fluids Struct.* **38**, 205–222.

FEILICH, K.L. & LAUDER, G.V. 2015 Passive mechanical models of fish caudal fins: effects of shape and stiffness on self-propulsion. *Bioinspir. Biomim.* **10** (3), 036002.

FEURTADO, P.A., CONLON, S.C. & SEMPERLOTTI, F. 2014 A normalized wave number variation parameter for acoustic black hole design. *J. Acoust. Soc. Am.* **136** (2), EL148–EL152.

FLORYAN, D. & ROWLEY, C.W. 2020 Distributed flexibility in inertial swimmers. *J. Fluid Mech.* **888**, A24.

FLORYAN, D., VAN BUREN, T., ROWLEY, C.W. & SMITS, A.J. 2017 Scaling the propulsive performance of heaving and pitching foils. *J. Fluid Mech.* **822**, 386–397.

GAZZOLA, M., ARGENTINA, M. & MAHADEVAN, L. 2014 Scaling macroscopic aquatic locomotion. *Nat. Phys.* **10** (10), 758–761.

GIBOUIN, F., RAUFASTE, C., BOURET, Y. & ARGENTINA, M. 2018 Study of the thrust–drag balance with a swimming robotic fish. *Phys. Fluids* **30** (9), 091901.

GODOY-DIANA, R., MARAIS, C., AIDER, J.-L. & WESFREID, J.E. 2009 A model for the symmetry breaking of the reverse Bénard–von Kármán vortex street produced by a flapping foil. *J. Fluid Mech.* **622**, 23–32.

GRAY, J. 1933 Studies in animal locomotion: I. The movement of fish with special reference to the eel. *J. Expl Biol.* **10** (1), 88–104.

GREEN, G. 1838 On the motion of waves in a variable canal of small depth and width. *Trans. Camb. Phil. Soc.* **6**, 457.

GUGLIELMINI, L. & BLONDEAUX, P. 2004 Propulsive efficiency of oscillating foils. *Eur. J. Mech.* B/*Fluids* **23** (2), 255–278.

HARIRI, H., BERNARD, Y. & RAZEK, A. 2013 A traveling wave piezoelectric beam robot. *Smart Mater. Struct.* **23** (2), 025013.

HULTMARK, M., LEFTWICH, M. & SMITS, A.J. 2007 Flowfield measurements in the wake of a robotic lamprey. *Exp. Fluids* **43** (5), 683–690.

KANCHARALA, A.K. & PHILEN, M.K. 2016 Optimal chordwise stiffness profiles of self-propelled flapping fins. *Bioinspir. Biomim.* **11** (5), 056016.

KIM, G.H., PARK, J.W. & JEONG, S.H. 2009 Analysis of dynamic characteristics for vibration of flexural beam in ultrasonic transport system. *J. Mech. Sci. Technol.* **23** (5), 1428–1434.

KÓSA, G., SHOHAM, M. & ZAAROOR, M. 2005 Propulsion of a swimming micro medical robot. In *Proceedings of the 2005 IEEE International Conference on Robotics and Automation*, pp. 1327–1331. IEEE.

KRAMERS, H.A. 1926 Wellenmechanik und halbzahlige quantisierung. *Z. Phys.* **39** (10–11), 828–840.

KRYLOV, V.V. & TILMAN, F.J.B.S. 2004 Acoustic 'black holes' for flexural waves as effective vibration dampers. *J. Sound Vib.* **274** (3–5), 605–619.

LADD, A.J.C. & VERBERG, R. 2001 Lattice-Boltzmann simulations of particle-fluid suspensions. *J. Stat. Phys.* **104** (5–6), 1191–1251.

LAGOPOULOS, N.S., WEYMOUTH, G.D. & GANAPATHISUBRAMANI, B. 2019 Universal scaling law for drag-to-thrust wake transition in flapping foils. *J. Fluid Mech.* **872**, R1.

LAUDER, G.V., ANDERSON, E.J., TANGORRA, J. & MADDEN, P.G.A. 2007 Fish biorobotics: kinematics and hydrodynamics of self-propulsion. *J. Expl Biol.* **210** (16), 2767–2780.

LENTINK, D., MUIJRES, F.T., DONKER-DUYVIS, F.J. & VAN LEEUWEN, J.L. 2008 Vortex-wake interactions of a flapping foil that models animal swimming and flight. *J. Expl Biol.* **211** (2), 267–273.

LEWIN, G.C. & HAJ-HARIRI, H. 2003 Modelling thrust generation of a two-dimensional heaving airfoil in a viscous flow. *J. Fluid Mech.* **492**, 339–362.

LIGHTHILL, M.J. 1960 Note on the swimming of slender fish. *J. Fluid Mech.* **9** (2), 305–317.

LIGHTHILL, M.J. 1970 Aquatic animal propulsion of high hydromechanical efficiency. *J. Fluid Mech.* **44** (2), 265–301.

LINDSEY, C.C. 1978 Form, function and locomotory habits in fish. In *Fish Physiology: Locomotion* (ed. WS Hoar & DJ Randall), pp. 1–100. Academic Press.

LIOUVILLE, J. 1836 Mémoire sur le développement des fonctions ou parties de fonctions en séries dont les divers termes sont assujétis à satisfaire à une même équation différentielle du second ordre, contenant un paramètre variable. *J. Math. Pures Appl.* **1**, 253–265.

LUO, Y., XIAO, Q., SHI, G., WEN, L., CHEN, D. & PAN, G. 2020 A fluid–structure interaction solver for the study on a passively deformed fish fin with non-uniformly distributed stiffness. *J. Fluids Struct.* **92**, 102778.

MAO, W. & ALEXEEV, A. 2014 Motion of spheroid particles in shear flow with inertia. *J. Fluid Mech.* **749**, 145–166.

MASOUD, H. & ALEXEEV, A. 2010 Resonance of flexible flapping wings at low Reynolds number. *Phys. Rev.* E **81** (5), 056304.

MASOUD, H. & ALEXEEV, A. 2012 Efficient flapping flight using flexible wings oscillating at resonance. In *Natural Locomotion in Fluids and on Surfaces* (ed. S. Childress, A. Hosoi, W.W. Schultz & J. Wang), pp. 235–245. Springer.

MASOUD, H., BINGHAM, B.I. & ALEXEEV, A. 2012 Designing maneuverable micro-swimmers actuated by responsive gel. *Soft Matt.* **8** (34), 8944–8951.

MICHELIN, S. & LLEWELLYN SMITH, S.G. 2009 Resonance and propulsion performance of a heaving flexible wing. *Phys. Fluids* **21** (7), 071902.

MINIKES, A., GABAY, R., BUCHER, I. & FELDMAN, M. 2005 On the sensing and tuning of progressive structural vibration waves. *IEEE Trans. Ultrason. Ferroelectr. Freq. Control* **52** (9), 1565–1576.

MIRONOV, M.A. 1988 Propagation of a flexural wave in a plate whose thickness decreases smoothly to zero in a finite interval. *Sov. Phys. Acoust.* **34** (3), 318–319.

MÜLLER, U.K. & VAN LEEUWEN, J.L. 2006 Undulatory fish swimming: from muscles to flow. *Fish Fisheries* **7** (2), 84–103.

NAUEN, J.C. & LAUDER, G.V. 2002 Hydrodynamics of caudal fin locomotion by chub mackerel, scomber japonicus (scombridae). *J. Expl Biol.* **205** (12), 1709–1724.

PARAZ, F., SCHOUVEILER, L. & ELOY, C. 2016 Thrust generation by a heaving flexible foil: resonance, nonlinearities, and optimality. *Phys. Fluids* **28** (1), 011903.

PELAT, A., GAUTIER, F., CONLON, S.C. & SEMPERLOTTI, F. 2020 The acoustic black hole: a review of theory and applications. *J. Sound Vib.* **476**, 115316.

RAMANANARIVO, S., GODOY-DIANA, R. & THIRIA, B. 2013 Passive elastic mechanism to mimic fish-muscle action in anguilliform swimming. *J. R. Soc. Interface* **10** (88), 20130667.

ROH, Y., LEE, S. & HAN, W. 2001 Design and fabrication of a new traveling wave-type ultrasonic linear motor. *Sensors Actuators* A **94** (3), 205–210.

SFAKIOTAKIS, M., LANE, D.M. & DAVIES, J.B.C. 1999 Review of fish swimming modes for aquatic locomotion. *IEEE J. Ocean. Engng* **24** (2), 237–252.

SMITS, A.J. 2019 Undulatory and oscillatory swimming. *J. Fluid Mech.* **874**, P1.

TANGORRA, J.L., LAUDER, G.V., HUNTER, I.W., MITTAL, R., MADDEN, P.G.A. & BOZKURTTAS, M. 2010 The effect of fin ray flexural rigidity on the propulsive forces generated by a biorobotic fish pectoral fin. *J. Expl Biol.* **213** (23), 4043–4054.

TIMOSHENKO, S. & WOINOWSKY-KRIEGER, S. 1959 *Theory of Plates and Shells*. McGraw-Hill.

TYTELL, E.D. 2010 Do trout swim better than eels? Challenges for estimating performance based on the wake of self-propelled bodies. In *Animal Locomotion* (ed. G.K. Taylor, M.S. Triantafyllou & C. Tropea), pp. 63–74. Springer.

TYTELL, E.D., BORAZJANI, I., SOTIROPOULOS, F., BAKER, T.V., ANDERSON, E.J. & LAUDER, G.V. 2010 Disentangling the functional roles of morphology and motion in the swimming of fish. *Integr. Compar. Biol.* **50** (6), 1140–1154.

TYTELL, E.D. & LAUDER, G.V. 2004 The hydrodynamics of eel swimming: I. Wake structure. *J. Expl Biol.* **207** (11), 1825–1841.

VAN EYSDEN, C.A. & SADER, J.E. 2006 Resonant frequencies of a rectangular cantilever beam immersed in a fluid. *J. Appl. Phys.* **100** (11), 114916.

VON ELLENRIEDER, K.D., PARKER, K. & SORIA, J. 2003 Flow structures behind a heaving and pitching finite-span wing. *J. Fluid Mech.* **490**, 129–138.

WEAVER, W. JR., TIMOSHENKO, S.P. & YOUNG, D.H. 1990 *Vibration Problems in Engineering*. John Wiley & Sons.

WEBB, P.W. 1994 The biology of fish swimming. In *Mechanics and physiology of animal swimming* (ed. L. Maddock, Q. Bone & J.M.V. Rayner), pp. 45–62. Cambridge University Press.

WENTZEL, G. 1926 Eine verallgemeinerung der quantenbedingungen für die zwecke der wellenmechanik. *Z. Phys.* **38** (6–7), 518–529.

WU, T.Y. 2011 Fish swimming and bird/insect flight. *Annu. Rev. Fluid Mech.* **43**, 25–58.

YEH, P.D. & ALEXEEV, A. 2014 Free swimming of an elastic plate plunging at low Reynolds number. *Phys. Fluids* **26** (5), 053604.

YEH, P.D. & ALEXEEV, A. 2016*a* Biomimetic flexible plate actuators are faster and more efficient with a passive attachment. *Acta Mechanica Sin.* **32** (6), 1001–1011.

YEH, P.D. & ALEXEEV, A. 2016*b* Effect of aspect ratio in free-swimming plunging flexible plates. *Comput. Fluids* **124**, 220–225.

YEH, P.D., DEMIRER, E. & ALEXEEV, A. 2019 Turning strategies for plunging elastic plate propulsor. *Phys. Rev. Fluids* **4**, 064101.

YEH, P.D., LI, Y. & ALEXEEV, A. 2017 Efficient swimming using flexible fins with tapered thickness. *Phys. Rev. Fluids* **2**, 102101.

ZHAO, L., CONLON, S.C. & SEMPERLOTTI, F. 2015 An experimental study of vibration based energy harvesting in dynamically tailored structures with embedded acoustic black holes. *Smart Mater. Struct.* **24** (6), 065039.